THE ASTRONOMICAL JOURNAL, 119:2166–2182, 2000 May


# STAR-FORMING REGIONS IN THE IRREGULAR GALAXY NGC 4449: DETERMINATION OF THEIR INTEGRATED PARAMETERS

ORIOL FUENTES-MASIP
Instituto de Astrofísica de Canarias, Calle Vía Láctea, E-38200 La Laguna, Tenerife, Spain; ofm@ll.iac.es
HÉCTOR O. CASTAÑEDA
Observatorio Astronómico Nacional, Universidad Nacional Autónoma de México, Apdo. Postal 877, 22860 Ensenada, BC, 22800 Mexico; hcastane@bufadora.astrosen.unam.mx
AND
CASIANA MUÑOZ-TUÑÓN
Instituto de Astrofísica de Canarias, Calle Vía Láctea, E-38200 La Laguna, Tenerife, Spain; cmt@ll.iac.es
*Received 1999 October 20; accepted 2000 February 9*

## ABSTRACT

We present a study of the H II regions in the central area of the giant irregular galaxy NGC 4449 based on observations taken on the William Herschel Telescope at the Roque de los Muchachos observatory with the Taurus II Fabry-Perot interferometer in the emission lines of Hα and [O III] 5006.8. We show that the usual methods of determining sizes of H II regions are not valid in this galaxy because of the high surface density of nebulae and the presence of an intense diffuse luminosity over NGC 4449, so it has been necessary to develop a new method. The procedure we have used allows integrated parameters of H II regions (radius, luminosity, radial velocity, and velocity dispersion) to be obtained with greater objectivity and precision than with other methods. The technique proposed here can be extended to parameterize giant H II regions in galaxies in general and to resolve the problem of the large uncertainties associated with previous methods in characterizing star-forming regions in Magellanic irregular galaxies.

*Key words:* galaxies: irregular — H II regions — Magellanic Clouds — techniques: spectroscopic

## 1. INTRODUCTION

Giant extragalactic H II regions (GEHRs) are areas of active star formation, ubiquitous in spiral and high-luminosity irregular galaxies, characterized by diameters greater than 100 pc, an average Hα luminosity of the order of $10^{39}$ ergs $s^{-1}$, an ionized gas mass of $10^4$–$10^5$ $M_\odot$, an average density of 1–10 $cm^{-3}$, and a population of 100 to 200 ionizing stars (Kennicutt 1984, 1988). However, none of these parameters can be used to differentiate them qualitatively from *normal* H II regions, except the velocity dispersion of the ionized gas, which is subsonic for the latter while supersonic for the former (Smith & Weedman 1970, 1971). These objects provide important clues to the problems of massive star formation and the chemical evolution of galaxies. They are also useful as secondary distance indicators, because of their large sizes and luminosities, in particular at intermediate distances, where stellar indicators are no longer observable (Sandage & Tammann 1974; Hodge 1976b; Smith 1977; Kennicutt 1979).

Discovered in the late 1970s, a correlation between the diameter or the luminosity and the supersonic velocity dispersion (Melnick 1977, 1979) for GEHRs became a promising tool, since the line width is easier to measure precisely and objectively as opposed to the luminosity and especially the diameter of the region, which were the only GEHR parameters used to determine distances. However, because establishing and using these correlations still required a precise determination of sizes and luminosities, it was necessary to find a method to measure both magnitudes reliably.

One of the most popular ways to measure sizes of nebulae was the *visual* method used by Sandage & Tammann (1974), Hodge (1976a, 1983), and Sabbandin & Bianchini (1979), among others. This method is based on visual inspection of the images and, although useful for some purposes, is clearly subjective and highly dependent on the exposure time or the observational technique. In a detailed study of this method, Kennicutt (1979) demonstrated that it gave rise to both stochastic and systematic errors when used by different authors, even in the same images.

Kennicutt (1979) himself proposed the isophotal method, assigning to the boundaries of halos and cores of H II regions mean Hα luminosities of $2 \times 10^{-16}$ and $2 \times 10^{-15}$ ergs $cm^{-2}$ $s^{-1}$ $arcsec^{-2}$, respectively. This method is objective but difficult to apply in general, given the wide variety of environments in which H II regions can be found. In particular, for many Magellanic irregular galaxies, the overlapping of H II region luminosity profiles and the diffuse nebular emission, which has an intensity comparable to the halos of isolated H II regions, makes this method unviable.

Regarding the separation of adjacent nebulae as physically independent entities, Gallagher & Hunter (1983) and Muñoz-Tuñón (1994) proposed using the fact that different H II regions usually present different kinematics. In this way, changes in radial velocity and/or velocity dispersion can be used to disentangle close nebulae. However, although this method may allow the discrimination of individual H II regions, it does not help to set their limits precisely.

We are conducting a study of the H II region population of irregular galaxies as part of a long-term program to study the use of the global population of H II regions in a single galaxy as distance indicators. This is the first of a series of papers addressing the problem of the precise determination of the H II region parameters.

To achieve these goals, as homogeneous a sample of GEHRs as possible has to be analyzed to compare and relate their integrated parameters. In a single galaxy all the nebulae are at the same distance and, by means of a Fabry-

Perot imaging interferometer, can be observed and analyzed in the same conditions. Fabry-Perot observations, moreover, provide morphological and kinematic information for all the points in the image simultaneously and with high spatial and spectral resolution.

The first target of our study and the object of the present work, NGC 4449, is a giant irregular galaxy ideally suited for this study. The absence of spiral arms provides us with a homogeneous H II region sample, as it has been shown that there are indications of statistical differences between the arm and interarm populations in spiral galaxies (Knapen et al. 1993 and references therein). Irregular galaxies often rotate slowly, thus restricting the radial velocity range and so simplifying the observation and analysis of their kinematics.

NGC 4449 is relatively nearby (we adopt here a distance of 5.0 Mpc following Sandage & Tammann 1975 and Aaronson & Mould 1983) and large (approximately 3′ diameter), which, together with its morphological classification, allows us to observe a large number of nebulae and, therefore, to carry out an analysis with statistical meaning. Table 1 presents the main physical parameters for this galaxy. The galaxy shows an abnormally high proportion of nebulae with supersonic velocity widths (Hartmann, Geller, & Huchra 1986), especially in its central areas, where our observations were performed, and so it is particularly suited to the study of the relationships between velocity dispersion and size or luminosity in GEHRs. The drawback is that the H II regions in the central areas of NGC 4449 are so close to one another that their luminosity profiles overlap, and so it is difficult to obtain their real sizes. Also, the intense emission of diffuse ionized gas makes it more difficult to set precise limits for the nebulae, especially because its brightness is far from constant, increasing while approaching the northeast-southwest axis of the galaxy.

This galaxy has been studied in the context of the gaseous and stellar content of irregular galaxies and the star formation processes in these systems, and there is a relatively large number of papers addressing these issues (see, e.g., Bothun 1986; Kennicutt, Edgar, & Hodge 1989; Sasaki, Ohta, & Saito 1990; Scowen 1992; Hill et al. 1994; Hunter & Gallagher 1997). Published works centered on the analysis of the kinematics of the ionized gas are, however, much more scarce (Sabbandin, Ortolani, & Bianchini 1984; Hartmann et al. 1986; Malumuth, Williams, & Schommer 1986), and, therefore, this is the core of the work that we present in this paper. In particular, a reliable, objective method for determining the integrated parameters of H II regions in galaxies such as NGC 4449, with such a high surface density of nebulae and such an intense diffuse luminosity, is lacking. This is necessary not only for analyzing the aforementioned correlations, but also for a statistical study of the H II region population in galaxies (especially when they present features similar to those in NGC 4449) regarding their luminosity function or their diameter distribution function.

In this paper we provide a catalog of the H II regions of the central area of the galaxy NGC 4449 with their associated parameters, as well as a discussion of the most suitable techniques to obtain them. A detailed discussion of the results and physical implications derived from the catalog will be the subject of a forthcoming paper.

## 2. OBSERVATIONS AND DATA REDUCTION

### 2.1. *Fabry-Perot Data*

Since our intention was to not only determine diameters and fluxes accurately, but also to associate velocity dispersions with these parameters, a Fabry-Perot imaging interferometer was the most suitable instrument. Unlike slit spectrometers, Fabry-Perot interferometers provide the spectra of all the points in a two-dimensional image simultaneously, with high spectral resolution and seeing-limited spatial resolution. In this way, the observational conditions for all the H II regions studied are exactly the same.

We used the Taurus II Fabry-Perot imaging spectrograph (Atherton & Taylor 1980) at the Cassegrain focus of the 4.2 m William Herschel Telescope at the Roque de los Muchachos observatory, during the nights of 1991 January 31 and February 1. The 125 $\mu$m etalon was used. The seeing was 1″. Four data cubes in the central 80″ × 80″ area (the richest in GEHRs; Hartmann et al. 1986) of NGC 4449 were obtained, two in the H$\alpha$ emission line and the other two in [O III] $\lambda$5006.8. Each pair of data cubes in a given wavelength were centered on different positions in the galaxy, with an overlapping area to check the results

TABLE 1

BASIC PHYSICAL PARAMETERS OF NGC 4449

| Parameter | Value | Reference |
|---|---|---|
| R.A. (1950) | $12^h\ 25^m\ 46^s$ | |
| Decl. (1950) | 44° 22′ 17″ | |
| Classification | Irr I | Sandage 1961 |
| Adopted distance | 5.0 Mpc | Sandage & Tammann 1975 |
| Angular size (H$\alpha$) | 3.′5 × 2.′5 | |
| Heliocentric radial velocity | $\sim$215 km s$^{-1}$ | Hartmann, Geller, & Huchra 1986 |
| H I mass | $10^{9.7}\ M_\odot$ | Hunter & Gallagher 1986 |
| $H_2$ mass | $\sim 10^8\ M_\odot$ | Sasaki, Ohta, & Saito 1990 |
| Dust mass | $\sim 1.5 \times 10^6\ M_\odot$ | Thronson et al. 1987 |
| Stars mass | $\sim 2 \times 10^{10}\ M_\odot$ | Gallagher, Hunter, & Tutukov 1984 |
| $B$ | −18.84 mag | Sandage & Tammann 1981 |
| $U-B$ | −0.30 mag | Hunter & Gallagher 1986 |
| $B-V$ | 0.41 mag | Hunter & Gallagher 1986 |
| 12 + log (O/H) | 8.5 ± 0.1 | Scowen 1992 |
| $L$(H$\alpha$) | $10^{41.0}$ ergs s$^{-1}$ | Hunter & Gallagher 1986 |
| Star formation rate | 1.5 $M_\odot$ yr$^{-1}$ | Thronson et al. 1987 |

obtained. These emission lines were selected because they are the brightest in H II regions. Besides, the [O III] 5006.8 Å line is more suited for kinematic studies because of its smaller thermal broadening. Interference filters with an FWHM of 15 Å and a central wavelength fitted to the galaxy Doppler shift were used to avoid the overlapping of the different interference orders.

The detector was an image photon counting system (IPCS), characterized by its null readout noise. The fast readout mode was used to average the eventual variations in atmospheric transmission during the integration. In this readout mode, the IPCS takes 10 ms to read one wavelength plane. In this way, the whole cube (100 planes) is scanned and read in less than 10 s. This procedure is continually repeated during the exposure time, which in our case was 1 hr for each data cube. The quantum efficiency of a CCD is of course much higher, but since it would have integrated the image corresponding to each etalon spacing only once, the differences in atmospheric transmission during the data cube integration time could have affected the line profiles. The resulting data format was $256 \times 256 \times 100$ (that is to say, 100 wavelength planes, each with $256 \times 256$ pixels). Later the format was limited to $245 \times 217 \times 100$ because of readout problems with the detector.

To avoid geometric distortions because of the detector, a pinhole-mask image was obtained at the beginning of each observing night. To monitor the changes in plate distance and optical axis position, calibration rings were obtained before and after each data cube. Also, a calibration cube was taken each night by observing a calibration lamp emission line. The reduction procedure was standard, using the TAUCAL package (Lewis & Unger 1991). Relevant data reduction and calibration parameters are listed in Table 2.

### 2.2. *Direct Imaging*

The IPCS data cubes were not flux-calibrated because the standard stars would have saturated the detector. The only way to solve this problem would have been to use a gray filter, but then the amount of light lost when observing NGC 4449 would have been unacceptable. So, to know the H II region flux, narrowband images were taken at the 1 m Jacobus Kapteyn Telescope in the same observatory during the nights of 1993 May 16 and 19. The detector used was the EEV7 CCD at the Cassegrain focus. The seeing was 1″ and the spatial scale was 0.″30 pixel$^{-1}$. The most relevant parameters are summarized in Table 3.

The images were reduced in the standard way for bias, flat field, and presence of cosmic rays, using the FIGARO package. Three images in each spectral line were obtained and later centered and averaged. The resultant Hα image was centered with respect to that taken in the adjacent continuum and the sky background was subtracted from both. The Hα continuum image was multiplied by the necessary factor to account for the differences in exposure times, filter width, and transmittance with respect to the Hα observations. Finally, the Hα continuum image was subtracted from that taken in Hα.

Because of the width of the filter used for the Hα images (60 Å), contamination due to [N II] 6548, 6584 Å emission lines was unavoidable. To correct this effect approximately, we used the value 0.12 for the quotient [N II]/Hα in NGC 4449 published by Kennicutt (1992). This value is an average for a slit placed along the northeast-southwest axis of this galaxy. In this way, our continuum-free Hα image was multiplied by the factor 0.89, which corresponds to the quotient Hα/(Hα + [N II]). After subtracting the sky background in the standard-star images, as well as in [O III], aperture photometry was applied in the standard way to get the calibration factors for Hα and [O III]. The correction for Galactic extinction was not made because in the direction to NGC 4449 it is negligible (Burstein & Heiles 1978; Hunter 1984).

The resulting narrowband images (continuum-free Hα and [O III] λ5006.8) are shown in Figure 1. Note that, apart from the difference in emission levels, both images are very similar. However, the Hα image shows apparently less diffuse emission than the one taken in [O III]. This must be due to the lack of continuum subtraction in the latter, since before the Hα data were continuum-subtracted, they also showed a diffuse component like that visible in the [O III] map. In fact, the image taken in the continuum adjacent to Hα displayed basically a smooth, diffuse structure whose brightness increased toward the center of the galaxy.

As a convenient, reliable way of estimating the errors in our photometry, we compared our data with available published work. The difference of our narrowband results in Hα compared with the NGC 4449 contour map published by Hunter (1982) is smaller than 15%, which we regard as a reliable measure of the average errors. The error estimation in the [O III] wavelength is more difficult because of the lack of published [O III] data for individual H II regions in this galaxy. Nevertheless, Kennicutt (1992) assigned the value of 0.57 for the quotient [O III]/(Hα + [N II]) in the integrated emission of this galaxy. To compare this value with our data, it is necessary to take into account that Kennicutt's [O III] data were continuum-free, while ours were not. The equivalent width given by Kennicutt in the same article for the integrated [O III] emission in NGC 4449 is 30 Å. Then, if his [O III] data included the continuum contribution, Kennicutt's value for the [O III]/(Hα + [N II]) quotient

TABLE 2

Data Reduction and Calibration Parameters

| Observational Parameters | Hα | [O III] |
|---|---|---|
| Rest wavelength (Å) | 6562.8 | 5006.8 |
| Calibration lamp wavelength (Å) | 6598.96 | 5037.75 |
| Interference filters central wavelength (Å) | 6562 | 5007 |
| Free spectral range (Å) | 13.36 | 7.78 |
| Free spectral range (km s$^{-1}$) | 610.1 | 465.6 |
| Wavelength increment per plane (Å) | 0.20 | 0.13 |
| Velocity increment per plane (km s$^{-1}$) | 9.11 | 7.70 |
| Calibration lamp FWHM (km s$^{-1}$) | 40 | 33 |
| Spatial scale (arcsec pixel$^{-1}$) | 0.26 | 0.26 |

TABLE 3

Most Relevant Parameters of the Direct Imaging Observations

| Object | Number of Images | Exposure Time (s) | Filter Central Wavelength (Å) | Filter Δλ (Å) |
|---|---|---|---|---|
| NGC 4449 | 3 | 1800 | 6569 | 60 |
| | 1 | 1200 | 6835 | 50 |
| | 3 | 1800 | 5012 | 50 |
| HZ 44 | 1 | 300 | 6569 | 60 |
| Feige 92 | 1 | 420 | 5012 | 50 |

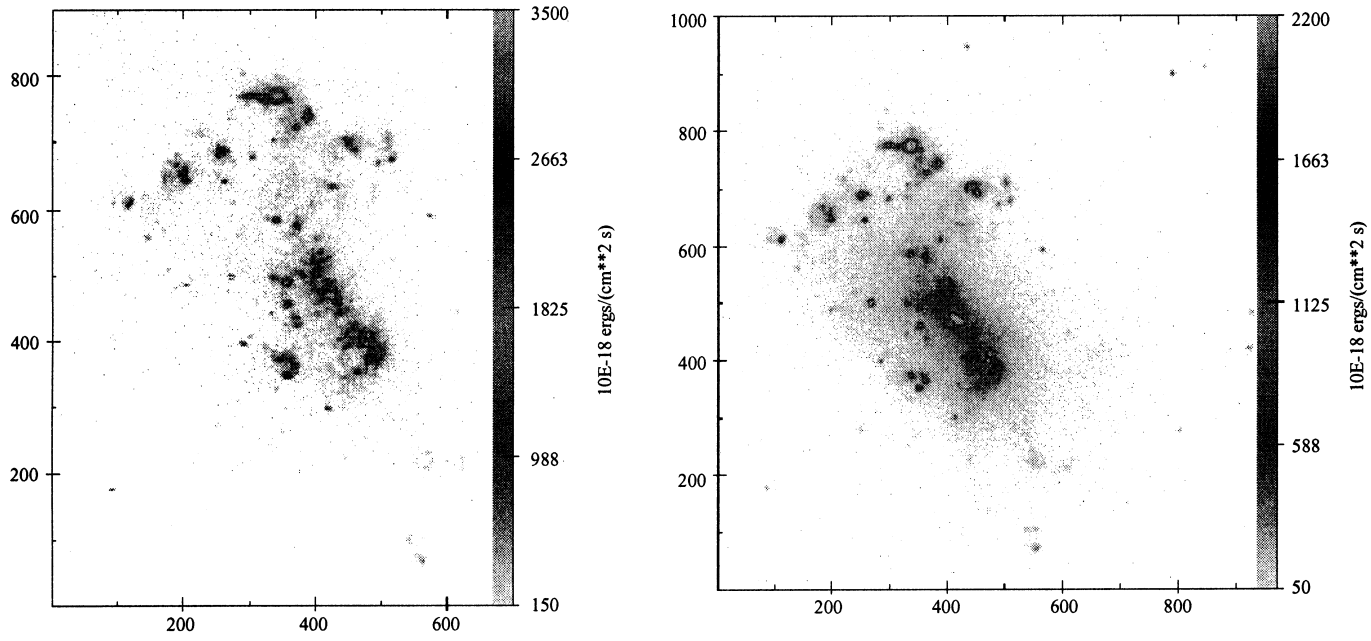


FIG. 1.—*Left*: NGC 4449 continuum-free flux map in Hα. *Right*: NGC 4449 [O III] flux map. In both panels, north is up and east is to the left. Units on the axis are pixels (1 pixel = 0.″30).

would be 0.59. This constitutes a perfect match with our results, which of course does not discard a photometry error of some 15% in our data, for consistency with Kennicutt's (1992) reported photometry errors and with the estimated error in our Hα data.

The calibration coefficients for the Hα Fabry-Perot data were obtained by comparing the continuum-free Hα image taken with the interferometer (obtained as described in § 3.1) with the corresponding narrowband one. Concerning the [O III] data, we measured the continuum emission in the Fabry-Perot data (see § 3.1) and made the necessary corrections to take into account that the continuum contribution was different in the wavelength ranges encompassed by the Fabry-Perot and the narrowband image. We assumed that the continuum level was constant along the small wavelength intervals involved (50 Å for the [O III] narrowband image and 7.8 Å for the free spectral range of the [O III] interferometer data). The difference in pixel size for both detectors was also taken into account for the two emission lines. The resulting calibration factors for the Fabry-Perot (adopting a distance of 5.0 Mpc to the galaxy) were $2.07 \times 10^{35}$ ergs $s^{-1}$ $count^{-1}$ for Hα and $4.89 \times 10^{34}$ ergs $s^{-1}$ $count^{-1}$ for [O III].

## 3. PROCEDURE FOR OBTAINING THE FABRY-PEROT MAPS

The analysis of the Fabry-Perot data was carried out mainly with MATADOR (Gavryusev & Muñoz-Tuñón 1996), a software package developed at the Instituto de Astrofísica de Canarias. The first step consisted in applying a Gaussian filter to our data cubes to increase their signal-to-noise ratio (S/N). The optimum width in the two spatial directions of the adopted filter was set at 2.5 pixels ($\sigma$) as a compromise between increasing the S/N and keeping the best possible spatial and spectral resolution.

### 3.1. *Continuum-free Flux Maps*

Once the filtered data cubes had been obtained, the emission in the 100 wavelength planes was added to produce the so-called collapsed maps, which are equivalent to narrowband images. To subtract the continuum emission, the spectra in each data cube were fitted with Gaussian profiles plus a continuum baseline (assumed to be of constant intensity, given the short wavelength range covered by the free spectral range of the interferometer, which is 13.36 Å for Hα and 7.78 Å for [O III]). The fitting parameters corresponding to each spectrum (such as the Gaussian amplitude above the continuum, its width, its central wavelength, and the mean continuum intensity) are stored to display its value for each of the points in the two-dimensional image, the respective maps being obtained in this way. The continuum-level map was then multiplied by the number of planes in the spectral direction and then subtracted from the collapsed map to obtain the continuum-free emission images.

The two images taken in each emission line were superposed to produce the global maps. The definitive images were built by trimming the data to remove the areas affected by "ghosts" (created by unavoidable, internal reflections in the Fabry-Perot interferometer, which were detected by comparing these images with those acquired at the Jacobus Kapteyn Telescope). The final maps are presented in Figure 2, where the reader's attention is drawn to the barred structure that constitutes the northeast-southwest axis of NGC 4449 and the diffuse emission increasing toward this axis.

### 3.2. *Radial Velocity and Velocity Dispersion Maps*

A masking technique was used to eliminate the low-S/N spectra in the areas outside the main body of the galaxy, which possess unreliable kinematic parameters. A first mask was made by selecting in the collapsed maps the emission levels that corresponded to spectra with S/Ns higher than 2, using the fact that the signal-to-noise map is proportional to the square root of the collapsed map, since the errors follow a Poisson law (Bland, Taylor, & Atherton 1987). A second mask, selecting the pixels whose spectra had been fitted with an amplitude error lower than 7% (which was

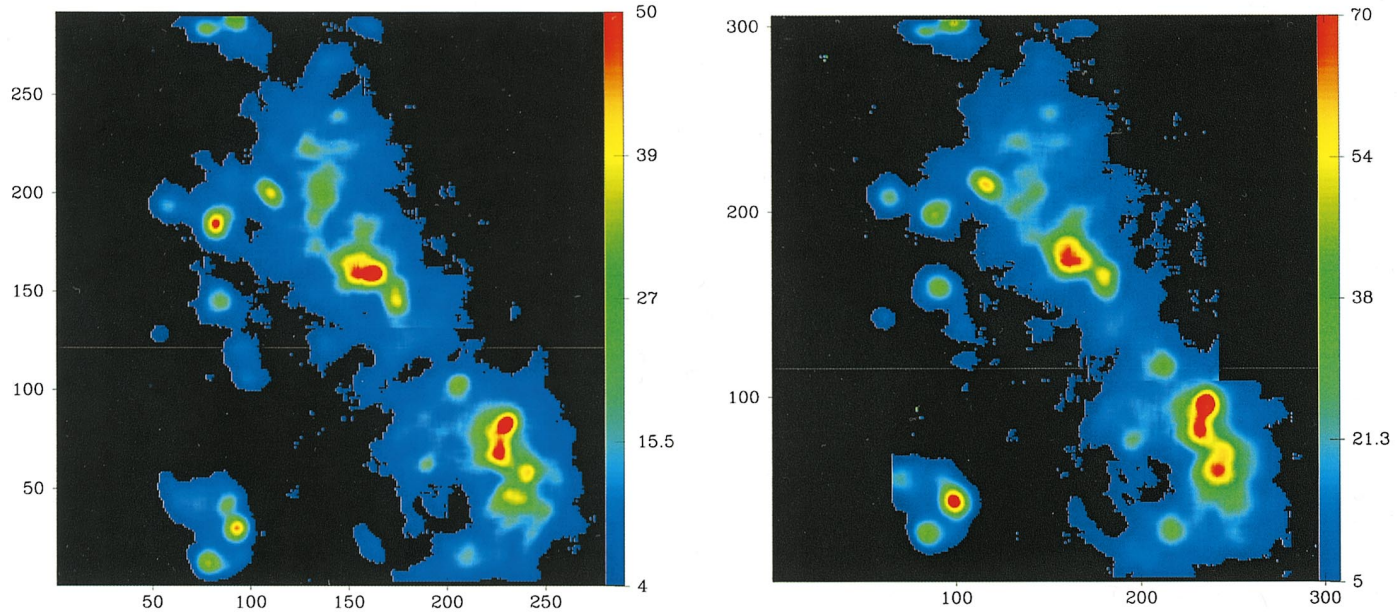


FIG. 2.—*Left*: Hα continuum-free emission map of NGC 4449. To convert this to ergs per square centimeter per second (the usual flux units), it should be multiplied by $6.9 \times 10^{-17}$ (an approximate calibration factor derived from the narrowband images). To get luminosity units (ergs per second), the corresponding factor is $2.1 \times 10^{35}$ (assuming a distance to NGC 4449 of 5.0 Mpc; Sandage & Tammann 1975; Aaronson & Mould 1983). *Right*: [O III] λ5006.8 continuum-free emission map of NGC 4449. To convert this to the usual flux units, it should be multiplied by $1.6 \times 10^{-17}$ (an approximate calibration factor derived from the narrowband images). To get luminosity units (ergs per second), the corresponding factor is $4.9 \times 10^{34}$ (assuming a distance to NGC 4449 of 5.0 Mpc; Sandage & Tammann 1975; Aaronson & Mould 1983). In both panels, north is up, east to the left, and units on the axis are pixels (1 pixel = 0″.26).

found to be the value equivalent to increasing the lower S/N threshold to $\gtrsim 3$) was used to produce still cleaner maps.

To obtain the final kinematic parameter maps, radial velocities were corrected to the heliocentric system of reference, and thermal (assuming a temperature of 10,000 K), instrumental, and (in the case of Hα) intrinsic broadenings were subtracted from the velocity dispersion to get the velocity dispersion due to mass motion (Muñoz-Tuñón 1994). In what follows, when we mention velocity dispersion or $\sigma$ we will be referring to this corrected line width, also known as the turbulent velocity dispersion. We present only the Hα kinematic parameter maps (Fig. 3) since the corresponding [O III] maps were very similar, showing essentially the same features.

In the radial velocity map, one can see the chaotic velocity field in the central area of this galaxy, with differences up to 50 km $s^{-1}$ between zones separated by some 200 pc. Radial velocities are relatively constant across individual H II regions, changing by less than 10 km $s^{-1}$. The whole range of radial velocities displayed in the map is about

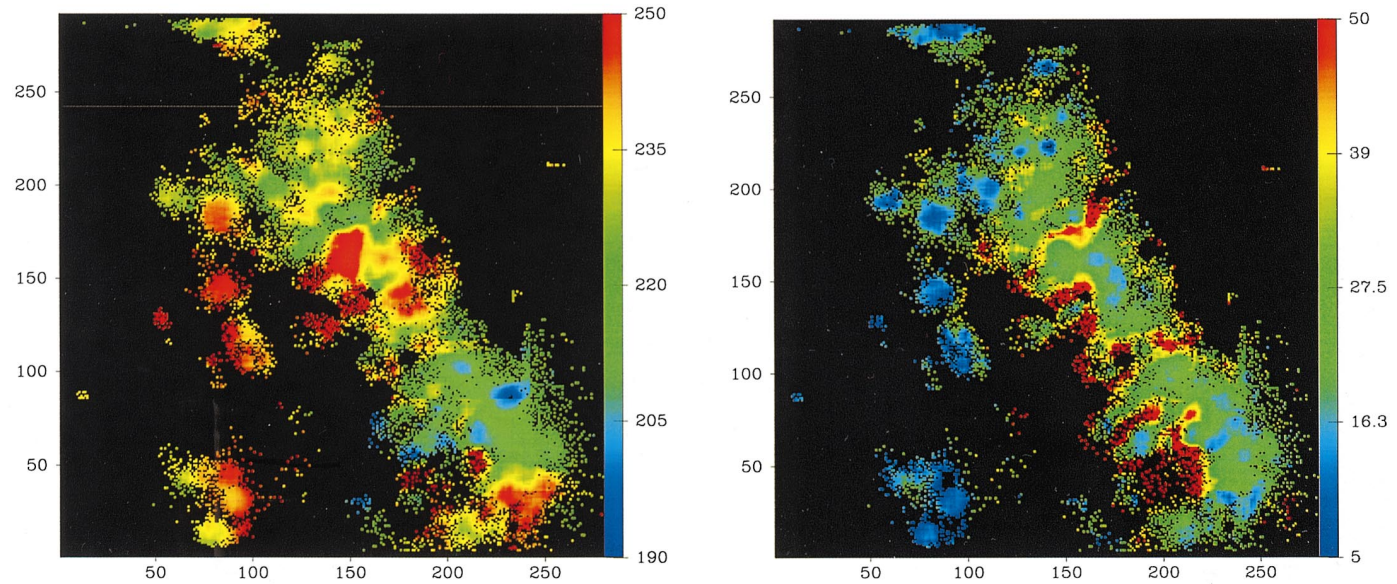


FIG. 3.—*Left*: Radial velocity map (in kilometers per second) for the central area of NGC 4449 in the Hα emission line. *Right*: Velocity dispersion ($\sigma$) map (in km $s^{-1}$) for the central area of NGC 4449 in the Hα emission line.

60 km $s^{-1}$. There is no indication of a rotation curve, and this is not due to the fact that we are observing only the central area, since it is also evident in the work by Yoshida et al. (1995), who cover a larger part of NGC 4449 with their H$\alpha$ map.

In the velocity dispersion map, H II regions typically display values of 10 to 20 km $s^{-1}$, significantly lower than the intercloud medium, which possesses values between 20 and 50 km $s^{-1}$. This difference can be attributed either to the blending of the emission of surrounding nebulae, each with a different radial velocity, or to the kinetic energy distribution, which produces a higher velocity dispersion in the diluted intercloud medium.

Almost all H II regions present supersonic $\sigma$, i.e., higher than some 13 km $s^{-1}$. The intense diffuse luminosity of NGC 4449 and its distance make the detection of smaller and fainter normal H II regions difficult, with subsonic velocity dispersion values. Data from Hartmann et al. (1986) show that outside the central area of NGC 4449, where the diffuse emission is less intense than in the center, the proportion of subsonic H II regions is higher.

## 4. DETERMINATION OF THE H II REGION PARAMETERS

In the Appendix we have revised most of the methods used in the literature to get the H II region parameters after having applied them to NGC 4449. We show that all of them present serious problems. Apart from subjectivity, the most important problems in getting realistic estimates of H II region sizes are the presence of the intense, diffuse emission (see Muñoz-Tuñón, Fuentes-Masip, & Castañeda et al. 1998 and references therein) and the overlapping of luminosity profiles in the areas with highest surface density of nebulae. Both these effects result in being able to see only the central, brightest areas of each nebulae, leading to an underestimate of their true dimensions. To solve these problems, it was necessary to find a method allowing the extrapolation of the brightest areas (not affected by the overlapping of luminosity profiles or by the diffuse emission) to lower flux levels. This method is described in §§ 4.1 and 4.2 and summarized in the flowchart presented in Figure 4.

### 4.1. *Diffuse Emission Subtraction*

The first step consisted in modeling the diffuse luminosity of NGC 4449 to subtract its contribution to the H II region emission, taking into account that its brightness is far from constant but increases toward the northeast-southwest axis of this galaxy. This was necessary to know the baseline to which the luminosity profile of each nebula was going to be extrapolated.

To model the diffuse luminosity, it must be separated from the H II region emission, but since the intensity of the former changes considerably with position, it is not possible to use a single isophote to distinguish between the two kinds of emission. For this reason, gradient maps were made from the continuum-free emission images in the same way as the radial velocity and velocity-dispersion gradient maps had been prepared (see the Appendix). The emission gradient maps tell us how the luminosity changes from pixel to pixel, the most abrupt variations corresponding to the H II regions themselves, because the diffuse-emission luminosity profile is comparatively smooth. Near the center of each nebula, the gradient values are again low, since the top of their luminosity profiles are relatively flat. By comparing maps of gradients with the continuum-free images, we find that the separation between H II regions and the diffuse luminosity is given by emission gradient values of 0.5 count $pixel^{-1}$, equivalent to $4.0 \times 10^{35}$ ergs $s^{-1}$ $arcsec^{-1}$ for H$\alpha$ and to $9.4 \times 10^{34}$ ergs $s^{-1}$ $arcsec^{-1}$ for [O III]. This value was used to make masks to eliminate the H II region emission in the continuum-free emission maps, isolating the diffuse luminosity contribution (shown in Fig. 5 for the H$\alpha$ emission line).

To model the diffuse luminosity, we used the IDL FITREGION routine, which allows two-dimensional polynomials to be fitted to arbitrarily shaped surfaces. This procedure made it possible to account for the spatial variation of the diffuse luminosity and to extrapolate it to the areas occupied by the H II regions.

The degree of the polynomial did not need to be very high, since the diffuse luminosity presents a smooth brightness profile, and it would have made no sense to use a polynomial that reproduced small-scale details. However, it was necessary to reproduce the global spatial structure of the diffuse luminosity. A four-by-four polynomial (fourth degree in each variable) was selected. The resulting fits are shown in Figure 6 for the H$\alpha$ data, on which intensity isocontours have been superposed.

By subtracting these fits from the continuum-free emission maps, we obtained images devoid of diffuse luminosity (Fig. 7, which also includes a finding chart for the H II region), showing the H II region emission clearly and exclusively. These maps, which did not contain the emission from the diffuse ionized gas (DIG), were used to extrapolate the nebular luminosity profiles to solve the problem posed by their overlapping in adjacent H II regions.

### 4.2. *Luminosity Profile Extrapolation and Integrated Parameter Determination*

The nebulae were detected by the Faint Object Classification and Analysis System (FOCAS) IRAF[1] package, using the methodology and input parameters described in § A3. FOCAS was applied to the DIG-free maps.

FOCAS performed some spurious detections at faint emission levels. By analyzing the detected features and by comparing with the Sabbandin & Bianchini (1979) and Hodge (1969) catalogs, we noticed that it was necessary to discard only the emission maxima with less than 2.3 for H$\alpha$ and 4.7 for [O III] counts in the brightest pixel. The detections performed in the maps area affected by Fabry-Perot ghosts were also discarded. In this way, 44 nebulae in H$\alpha$ and 24 in [O III] were positively detected. The difference is due to the slightly different areas covered by the observations in each emission line and to the fact that some nebulae do not show measurable emission in [O III] above the diffuse luminosity of this galaxy. The detection level was some 50% lower than that of Sabbandin & Bianchini (1979) for the same area because of the detector used.

Once the diffuse luminosity contribution had been subtracted and the nebulae had been detected, we had to extrapolate their luminosity profiles to get reliable estimates of their sizes, despite the overlapping of adjacent H II

[1] IRAF is distributed by the National Optical Astronomy Observatories, which are operated by the Association of Universities for Research in Astronomy, Inc., under cooperative agreement with the National Science Foundation.

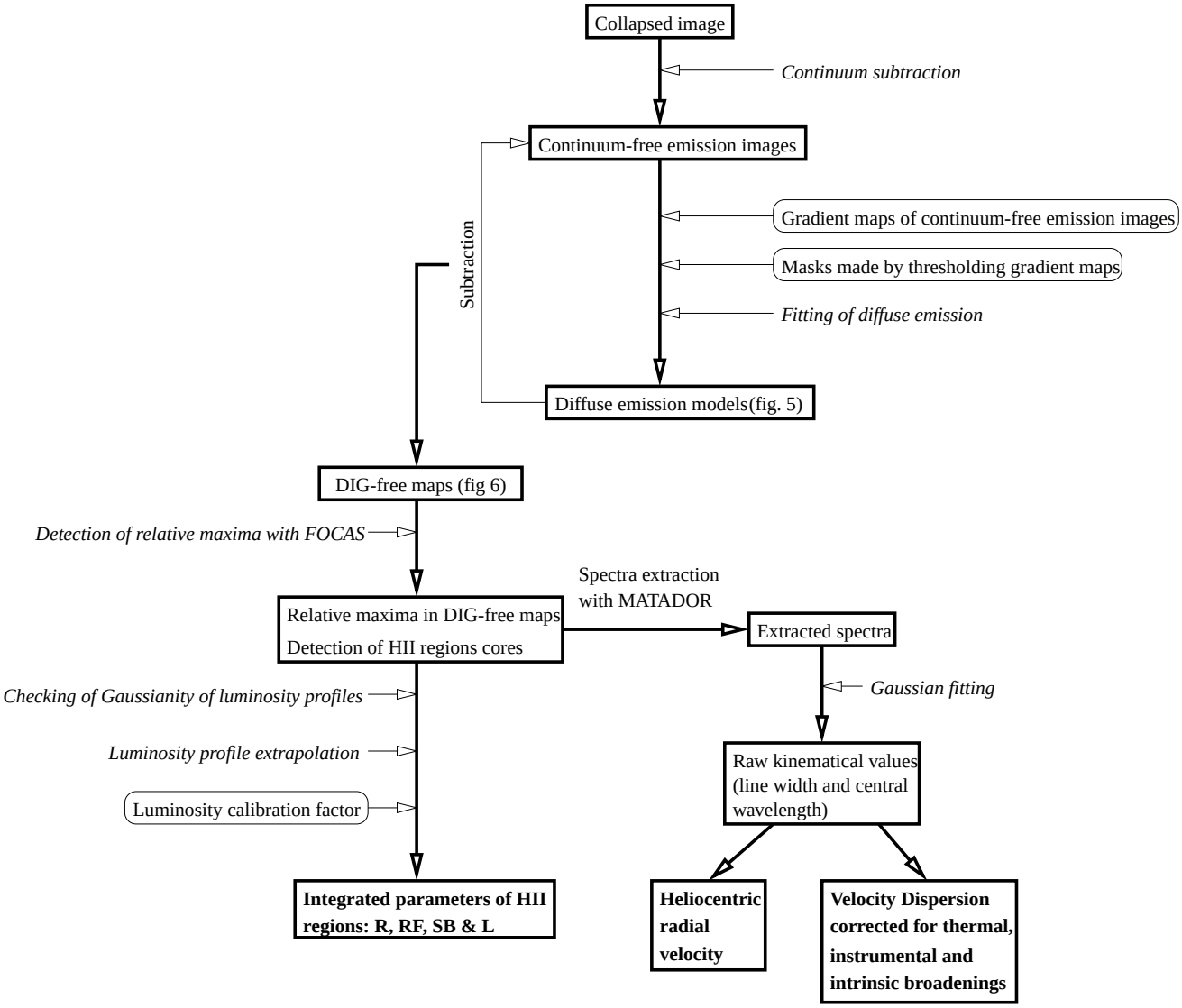


FIG. 4.—Flow chart summarizing the adopted process to obtain the H II region parameters. Heavy arrows and boxes with heavy borders indicate intermediate results and the path followed from the collapsed images to the determination of the H II region parameters (*bold text*). Light text and light arrows indicate auxiliary steps necessary to obtain some of the intermediate results (*ovals*).

regions. First, we checked if it was reasonable to extrapolate the luminosity profiles of the H II regions in our sample. With this aim, we extracted the luminosity profiles of isolated H II regions, located in areas where the diffuse emission was less intense. As can be seen in the examples shown in Figure 8, these profiles were almost perfectly Gaussian. Real luminosity profiles are clearly far from Gaussian (see, e.g., Kennicutt 1979), but given the distance to NGC 4449 and the convolution with the seeing and with the filter applied to the data to increase the S/N, this is not a surprising result, and the same would happen for all but the nearest galaxies.

To obtain the dimensions of the H II regions, it was necessary to take into account the seeing broadening and the effect caused by the filter applied to the data cubes to increase their S/N, which further broadened the luminosity profiles. Both the seeing and the filter profiles are Gaussian, and since their convolution with the true H II region luminosity profiles is also a Gaussian, we therefore assume that this true profile can be approximated by the same kind of function.

In this way, the observed profiles, $G_{\rm obs}(x, y)$, result from the convolution of three Gaussians: the real one (as we will later justify, we are assuming that it has the same standard deviation in the $x$ and $y$ axes), that due to the seeing, and that due to the filter (with subscripts $r$, $s$, and $f$, respectively), or

$$G_{\rm obs}(x, y) = 4\pi^2 I_r I_s I_f \frac{\sigma_r^2 \sigma_s^2 \sigma_f^2}{\sigma_r^2 + \sigma_s^2 + \sigma_f^2} e^{-(x^2+y^2)/2(\sigma_r^2+\sigma_s^2+\sigma_f^2)} .$$

Of course, the total flux of a given H II region (the volume under each Gaussian) is not affected by the seeing or filter convolutions (that is to say, the seeing and filter Gaussians have a volume equal to unity). Using this fact, the real luminosity profile of one of these hypothetical circular nebulae is

$$G_r(x, y) = \frac{l\sigma_{\rm obs}^2}{\sigma_{\rm obs}^2 - \sigma_s^2 - \sigma_f^2} e^{-(x^2+y^2)/2(\sigma_{\rm obs}^2-\sigma_s^2-\sigma_f^2)} ,$$

where $\sigma_{\rm obs}$ is the standard deviation of the observed profile and $l$ is the number of counts of the brightest pixel (the

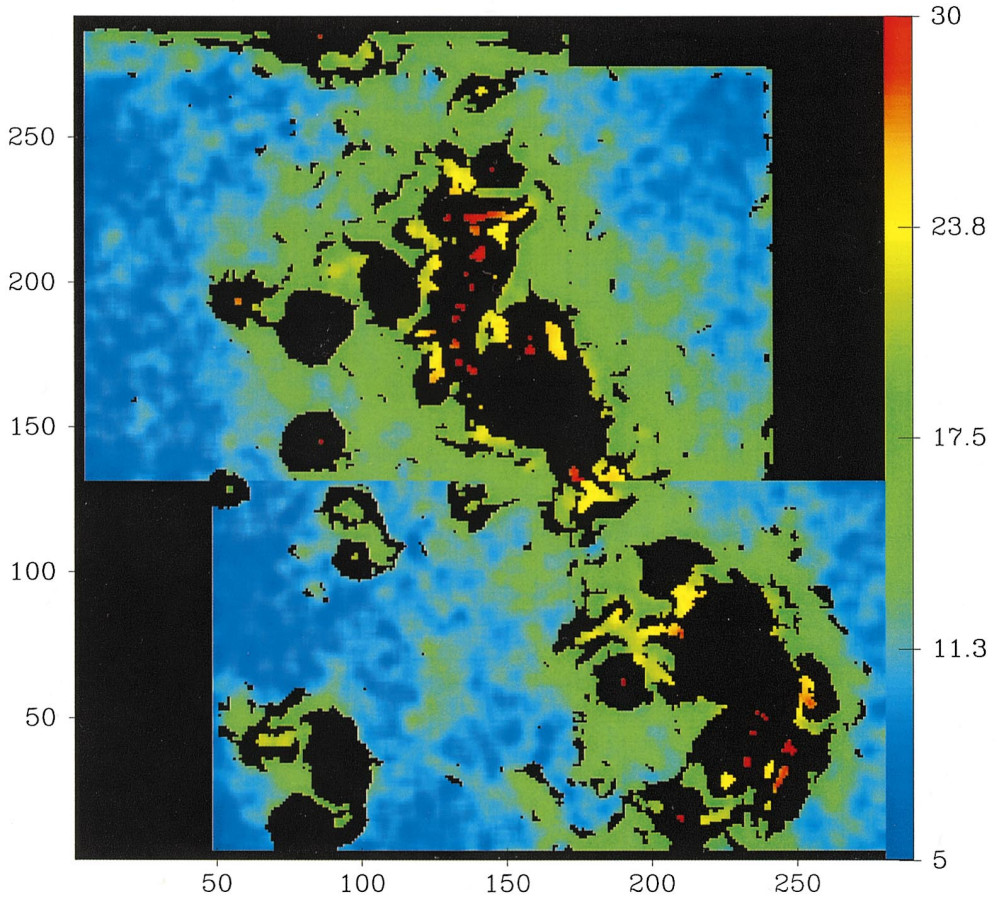


FIG. 5.—Hα diffuse luminosity in NGC 4449 after subtraction of the H II region contribution

central one) in the continuum-free emission map once the diffuse luminosity has been subtracted.

To obtain the real luminosity profile from the data provided by FOCAS, it must be taken into account that the area, $A$, given for each H II region found is limited by the isophote with mean count level, $i$, at which the nebula was detected. Hence,

$$i = le^{-r_{\rm FOC}^2/2\sigma_{\rm obs}^2} ,$$

which implies

$$\sigma_{\rm obs}^2 = \frac{r_{\rm FOC}^2}{2(\ln l - \ln i)} ,$$

where $r_{\rm FOC} = (A/\pi)^{1/2}$. In this way, $r_{\rm FOC}$ is the average, in all directions, of the radius of each nebula for the isophote level $i$ and is more representative of their size than any other parameter. This is the reason we are assuming Gaussians with the same standard deviation in the $x$ and $y$ axes.

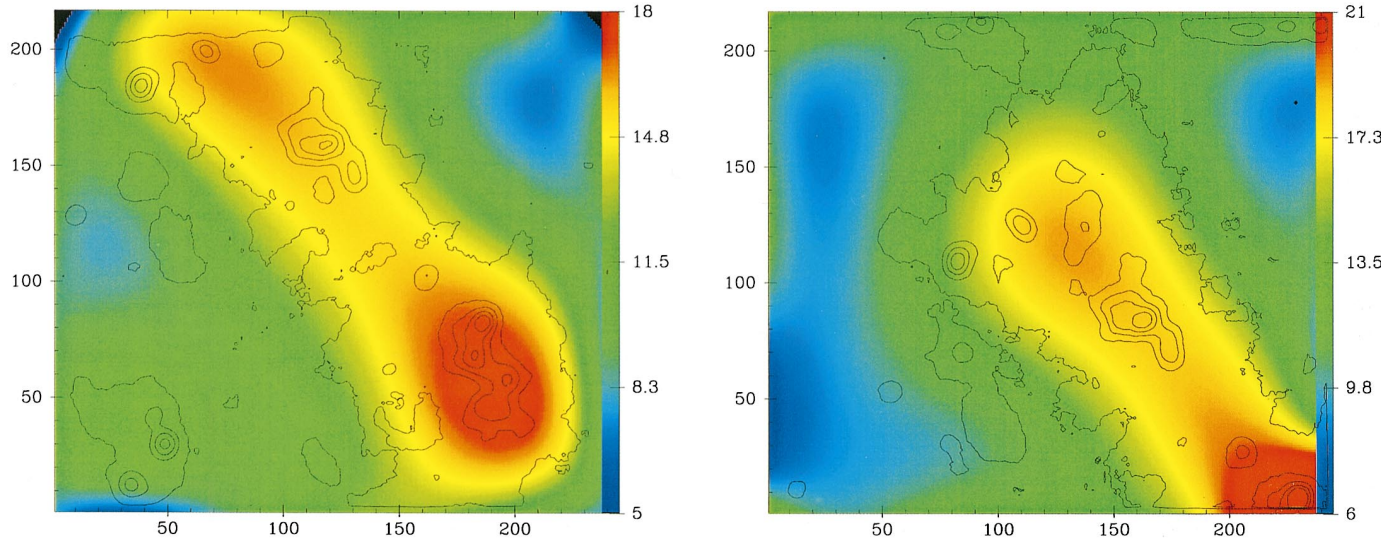


FIG. 6.—Diffuse luminosity models for the two Hα data cubes. The contours represent the continuum-free emission.

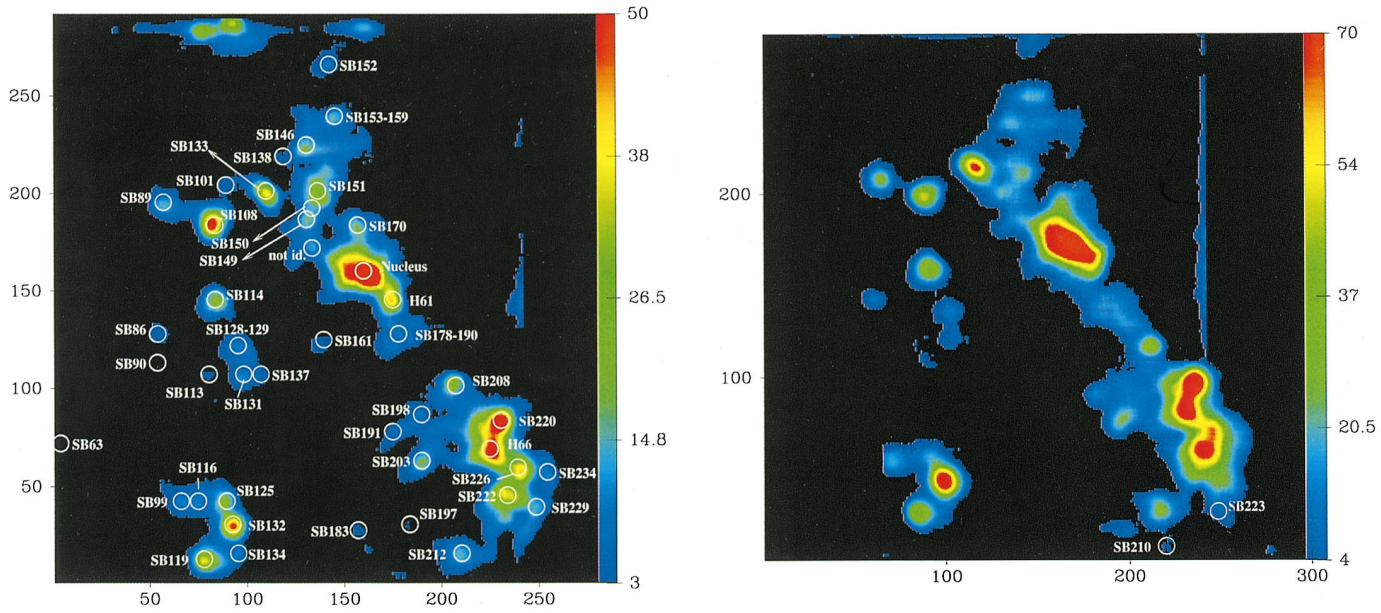


FIG. 7.—*Left*: Continuum-free Hα emission for the NGC 4449 H II regions after subtracting the diffuse luminosity. To get flux units (ergs per square centimeter per second), the map has to be multiplied by $6.9 \times 10^{-17}$ (an approximate calibration factor derived from direct imaging). A finding chart for the H II regions detected in Hα has been superposed. *Right*: Continuum-free [O III] emission for the NGC 4449 H II regions after subtracting the diffuse luminosity. To get flux units (ergs per square centimeter per second), the map has to be multiplied by $1.6 \times 10^{-17}$ (an approximate calibration factor, derived from direct imaging). A finding chart for the two H II regions that were detected in [O III] but not in Hα has been superposed.

It is now possible to determine the radius for a given section at any count level for a real luminosity profile. We decided to obtain two different radii for each nebula, one corresponding to a count level 3 times higher than the standard deviation of the local background and one corresponding to the half-width at half-maximum of the real luminosity profile. The former is designed to reproduce the size that would be observed for a hypothetical isolated H II region, located in a background devoid of diffuse emission. The latter is a measure less affected by small extrapolation or diffuse luminosity subtraction errors.

The radius $R$ at a count level 3 times higher than the standard deviation of the local background is given by

$$R = \left( \frac{[r_{\rm FOC}^2 - 2\sigma_{\rm sf}^2(\ln l - \ln i)]}{\ln l - \ln i} \times (\ln l r_{\rm FOC}^2 - \ln \{3\sigma_b [r_{\rm FOC}^2 - 2\sigma_{\rm sf}^2(\ln l - \ln i)]\}) \right)^{1/2},$$

where $\sigma_b$ is the standard deviation of the local background and $\sigma_{\rm sf}^2 \equiv \sigma_s^2 + \sigma_f^2$.

The radius $R_F$ corresponding to the half-width at half-maximum of the real luminosity profile is

$$R_F = \sqrt{2 \ln 2 \left[ \frac{r_{\rm FOC}^2}{2(\ln l - \ln i)} - \sigma_{\rm sf}^2 \right]}.$$

To define the surface brightness for nebulae, we could not divide the flux (volume enclosed by the luminosity profile) by the surface, since the former is limited, but the Gaussian surface is not. Therefore, we decided to limit the area in the $(x, y)$-plane by using the circular area with radius $R_F$ instead of that corresponding to $R$, to minimize the effect of extrapolation or diffuse-luminosity subtraction errors.

So, dividing the flux enclosed within the circle of radius

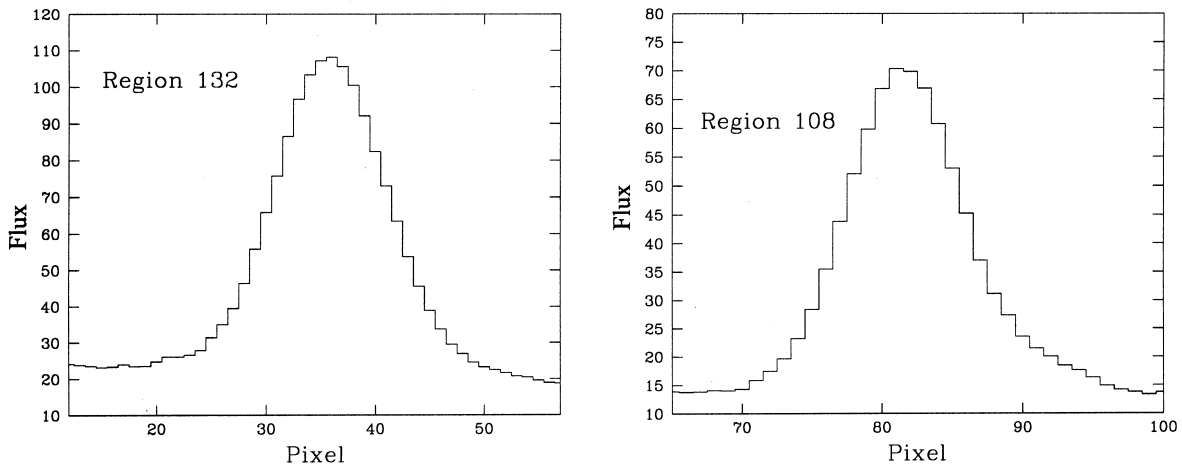


FIG. 8.—Examples of luminosity profiles for isolated H II regions located where the diffuse emission of NGC 4449 was less intense

$R_F$ by the area of this circle, we obtain a surface brightness (SB) given by

$$\mathrm{SB} = \frac{l r_{\mathrm{FOC}}^2}{2 \ln 2 [r_{\mathrm{FOC}}^2 - 2\sigma_{\mathrm{sf}}^2 (\ln l - \ln i)]} .$$

Finally, the luminosity for each H II region can be defined as the total volume enclosed by the two-dimensional Gaussian that represents its luminosity profile. This volume is the same for both the observed profile and the real one, and in this way

$$L = 2\pi l \sigma_{\mathrm{obs}}^2 = \frac{\pi l r_{\mathrm{FOC}}^2}{\ln l - \ln i} .$$

Luminosity values in ergs per second were calculated by means of the conversion factors derived from the flux-calibrated NGC 4449 images (see § 2.2). The values for $R$, $R_F$, $L$, and SB for the H II regions located in the areas where the two data cubes taken in each spectral line overlapped were obtained separately and later averaged. The differences between the two data cubes for these parameters were always below 20%. The mean difference (averaging all the H II regions found in the overlapping area, both in Hα and in [O III], since no systematic differences were observed between the two emission lines) for $R$ was 8%; for $R_F$, 5%; for $L$, 10%; and for SB, 12%.

Following this procedure, we obtained the values for the nebular integrated parameters as if they did not overlap, the diffuse luminosity did not exist, and their luminosity profiles had not been broadened by the seeing or by the filter applied to the data cubes.

To obtain the kinematic parameters of each nebula, it had to be taken into account that if we extracted the spectrum from the area determined after the luminosity profile extrapolation, the kinematic contribution from adjacent H II regions would affect the velocity dispersion and radial velocity values. However, if we restricted the spectrum extraction to the areas detected by FOCAS (that is, the brightest part of each luminosity profile, presumably not affected by neighboring H II regions), we wanted to know up to what point the kinematic parameters derived in this way were representative of the whole nebula. In other words, was it possible that the velocity dispersion values changed significantly if H II regions had been effectively isolated and we had been able to extract the integrated spectra from their whole area? Results of Sabalisck et al. (1995) and Muñoz-Tuñón et al. (1996) suggest the opposite. These authors found that the integrated velocity dispersion is highly dominated by the brightest part of the nebula. To check the validity of this assertion in our data, we extracted integrated spectra in concentric square areas for several isolated nebulae, beginning in the brightest area and increasing the size of the square until all the emission for each H II region was included. For areas larger than 5 × 5 pixels (equivalent to 1.″3 × 1.″3), the velocity dispersion variation is small (less than some 3 km s$^{-1}$). Although the kinematic parameters in a given H II region change with position across its surface (Muñoz-Tuñón 1994; Hippelein 1986), it is logical that such variations are difficult to observe except for the nearest objects because of the lack of spatial resolution. Therefore we can conclude that taking the brightest-area spectrum as representative for the whole H II region does not produce important errors.

The spectra extracted from the areas detected by FOCAS for each nebula were fitted with single Gaussians. The resulting velocity dispersions were corrected by instrumental, thermal (assuming a temperature of 10,000 K), and (in the case of Hα) intrinsic broadenings. Radial velocities were referred to the heliocentric system of reference. When an H II region was located in the overlapping area of the data cube, the two respective spectra were extracted, and radial velocities and velocity dispersions were averaged. The radial velocity differences found between the two data cubes were smaller than 5 km s$^{-1}$ (some 2%) in Hα and smaller than 10 km s$^{-1}$ (some 5%) in [O III]. The velocity dispersion differences were always below 4.5 km s$^{-1}$ and for most H II regions were smaller than 2 km s$^{-1}$ (or 10% of the line width) in both emission lines.

## 5. THE RESULTING CATALOG

The integrated parameters of the H II regions in the central area of NGC 4449 are shown in Tables 4 and 5. The H II region identification number in both tables is taken from Sabbandin & Bianchini (1979), except for regions h61 and h66, not detected by these authors, but present in Hodge's (1969) catalog. The region labeled "none" ("no identification") was found by Sabbandin & Bianchini (1979) but lacked clear identification in their work. Our region 128–129 comprises two of the nebulae found by Sabbandin & Bianchini, as well as the regions 153–159 and 178–190, although this duality should be interpreted with caution, since their spatial resolution is comparable to ours. In fact, Scowen (1992) also finds a single nebula at the position of regions 128 and 129 and detects the region 153 but does not find the region 159.

The H II region labeled "Nucleus" corresponds to the brightest point in NGC 4449. It must be taken into account that for an irregular galaxy without noticeable rotation, it is difficult to define a proper nucleus. However, the images of the continuum adjacent to Hα taken with the Jacobus Kapteyn Telescope do confirm this point as being the real nucleus of the galaxy. In those images, this point is far brighter than any other in NGC 4449 because of its high stellar density, as expected for the galactic nucleus.

In both tables, most of the H II regions display a supersonic velocity dispersion. Since the limiting value between the subsonic and supersonic velocity widths was set equal to 12.8 km s$^{-1}$, only regions 125 and 134 are clearly subsonic, whereas regions 86, 114, 119, 131, and 132 are near the limit. The average turbulent velocity dispersion value is some 20 km s$^{-1}$. In some cases, the high velocity width is due to fitting an asymmetric or split profile with a single Gaussian.

The radius $R$ (radius at a level 3 times higher than the standard deviation of the local background) ranges from ∼13 pc for region 138 to more than 100 pc for the nucleus. The mean value is near 65 pc. The extrapolation of luminosity profiles in general provided larger radii than those determined by other methods, especially in the most crowded areas or in those where the diffuse emission was most intense. For example, region h66 increased its size by a factor of ∼4 with respect to that found by FOCAS. On the other hand, more isolated regions, such as 89, 133, or 212, show basically the same size with any method.

The radius $R_F$ (corresponding to the half-width at half-maximum of the real luminosity profile) ranges from ∼6 pc for nebula 138 to values some 10 times larger for regions like the galactic nucleus. The mean value is around 35 pc.

TABLE 4

INTEGRATED H II REGION PARAMETERS FOR THE Hα DATA

| Identification | $v_{rad}$ (km s$^{-1}$) | $\sigma$[a] (km s$^{-1}$) | $R$[b] (pc) | $R_F$[c] (pc) | log SB[d] (ergs s$^{-1}$ pc$^{-2}$) | log $F$[e] (ergs s$^{-1}$ cm$^{-2}$) | log $L$[f] (ergs s$^{-1}$) |
|---|---|---|---|---|---|---|---|
| 63 ..... | 224.6 | 14.0 | 19.9 | 10.6 | 35.07 | −13.56 | 37.92 |
| 86 ..... | 235.8 | 8.2 | 26.0 | 13.9 | 35.07 | −13.33 | 38.15 |
| 89 ..... | 217.2 | 14.6 | 66.3 | 38.2 | 34.92 | −12.59 | 38.89 |
| 90 ..... | 227.6 | 18.7 | 25.8 | 22.6 | 34.39 | −13.58 | 37.90 |
| 99 ..... | 211.9 | 17.2 | 53.4 | 35.0 | 34.73 | −12.86 | 38.61 |
| 101 ..... | 213.5 | 22.6 | 29.8 | 20.5 | 34.63 | −13.42 | 38.06 |
| 108 ..... | 230.6 | 14.1 | 60.3 | 26.6 | 35.55 | −12.27 | 39.20 |
| 113 ..... | 237.7 | 16.1 | 21.4 | 11.2 | 35.10 | −13.48 | 37.99 |
| 114 ..... | 235.3 | 12.6 | 57.4 | 31.5 | 35.02 | −12.66 | 38.82 |
| 116 ..... | 219.0 | 16.4 | 55.1 | 36.6 | 34.71 | −12.84 | 38.63 |
| 119 ..... | 213.7 | 11.0 | 61.2 | 29.0 | 35.36 | −12.39 | 39.09 |
| 125 ..... | 225.2 | 3.9 | 53.0 | 27.6 | 35.14 | −12.66 | 38.81 |
| 128–129..... | 229.1 | 16.8 | 65.0 | 41.2 | 34.78 | −12.67 | 38.80 |
| 131 ..... | 232.0 | 11.4 | 44.6 | 25.5 | 34.94 | −12.93 | 38.55 |
| 132 ..... | 221.9 | 11.4 | 54.4 | 24.1 | 35.56 | −12.36 | 39.12 |
| 133 ..... | 213.4 | 16.4 | 52.5 | 23.8 | 35.47 | −12.46 | 39.02 |
| 134 ..... | 225.8 | 3.7 | 37.8 | 23.0 | 34.84 | −13.11 | 38.36 |
| 137 ..... | 232.3 | 19.9 | 37.9 | 23.3 | 34.80 | −13.14 | 38.33 |
| 138 ..... | 219.7 | 17.2 | 13.2 | 6.2 | 35.40 | −13.70 | 37.77 |
| 146 ..... | 220.3 | 17.4 | 77.3 | 44.0 | 34.93 | −12.46 | 39.02 |
| 149 ..... | 204.1 | 26.3 | 45.6 | 27.8 | 34.83 | −12.96 | 38.51 |
| 150 ..... | 221.4 | 27.9 | 63.6 | 36.1 | 34.93 | −12.63 | 38.85 |
| 151 ..... | 222.2 | 27.7 | 88.8 | 46.9 | 35.08 | −12.26 | 39.22 |
| 152 ..... | 221.3 | 13.7 | 39.1 | 23.7 | 34.82 | −13.11 | 38.37 |
| 153–159..... | 219.2 | 22.4 | 49.3 | 27.2 | 34.99 | −12.82 | 38.66 |
| 161 ..... | 240.5 | 29.5 | 30.6 | 20.3 | 34.72 | −13.36 | 38.12 |
| 170 ..... | 214.0 | 42.1 | 56.8 | 31.4 | 35.00 | −12.69 | 38.79 |
| 178–190..... | 228.3 | 19.2 | 38.6 | 22.6 | 34.90 | −13.07 | 38.40 |
| 183 ..... | 181.8 | 18.4 | 25.5 | 18.0 | 34.63 | −13.54 | 37.94 |
| 191 ..... | 201.9 | 27.7 | 41.6 | 27.2 | 34.73 | −13.08 | 38.40 |
| 197 ..... | 188.8 | 15.6 | 16.3 | 9.4 | 34.93 | −13.80 | 37.68 |
| 198 ..... | 211.6 | 32.8 | 60.7 | 40.9 | 34.71 | −12.74 | 38.74 |
| 203 ..... | 188.6 | 20.6 | 56.6 | 31.5 | 35.00 | −12.68 | 38.79 |
| 208 ..... | 197.6 | 23.0 | 52.8 | 25.5 | 35.30 | −12.56 | 38.91 |
| 212 ..... | 212.3 | 22.0 | 74.6 | 45.1 | 34.85 | −12.52 | 38.95 |
| 220 ..... | 183.4 | 19.3 | 74.3 | 32.4 | 35.61 | −12.05 | 39.43 |
| 222 ..... | 208.3 | 26.6 | 101.8 | 50.9 | 35.23 | −12.04 | 39.44 |
| 226 ..... | 198.0 | 20.7 | 73.4 | 34.8 | 35.37 | −12.23 | 39.25 |
| 229 ..... | 221.7 | 18.0 | 55.6 | 32.5 | 34.91 | −12.75 | 38.73 |
| 234 ..... | 194.1 | 24.1 | 43.2 | 26.9 | 34.80 | −13.02 | 38.46 |
| h 61 ..... | 227.1 | 19.3 | 85.9 | 41.8 | 35.30 | −12.14 | 39.33 |
| h 66 ..... | 195.2 | 21.5 | 108.1 | 50.7 | 35.39 | −11.87 | 39.60 |
| Nucleus..... | 230.3 | 25.9 | 112.9 | 49.0 | 35.61 | −11.68 | 39.79 |
| None. ..... | 213.2 | 34.2 | 35.5 | 21.8 | 34.80 | −13.20 | 38.27 |

[a] Velocity dispersion.
[b] Radius at a level 3 times higher than the standard deviation of the local background.
[c] Radius corresponding to the half-width at half-maximum of the luminosity profile.
[d] Logarithm of the surface brightness.
[e] Logarithm of the flux.
[f] Logarithm of the luminosity.

The fact that the quotient of $R$ and $R_F$ changes from 1.18 for region 178–190 in [O III] to 2.30 for the nucleus in Hα is an indication of the wide variety of luminosity profiles in H II regions (see, for example, Kennicutt 1979).

The range of surface brightness spans more than a factor of 10 and, in the case of luminosity, differences of 2 orders of magnitude are found. Mean values in Hα are around $10^{35.0}$ ergs s$^{-1}$ pc$^{-2}$ and $10^{38.8}$ ergs s$^{-1}$, respectively. In the [O III] data, corresponding mean values are $10^{34.6}$ ergs s$^{-1}$ pc$^{-2}$ and $10^{38.6}$ ergs s$^{-1}$.

Using the determined integrated parameters shown in Tables 4 and 5, we can calculate the luminosity function and the accumulated diameter distribution function for our sample of H II regions. Both functions have been widely used to study the statistical properties of the H II region population in galaxies (see, for example, Hodge 1983; Kennicutt et al. 1989). In our case, the luminosity function and, especially, the accumulated diameter distribution function (since it is less affected by having a relatively small number of available H II regions) are useful for checking the consistency of the method used to determine nebular parameters.

The accumulated diameter distribution function was cal-

TABLE 5

INTEGRATED H II REGION PARAMETERS FOR THE [O III] DATA

| Identification | $v_{rad}$ (km s$^{-1}$) | $\sigma$ (km s$^{-1}$) | $R$ (pc) | $R_F$ (pc) | log SB (ergs s$^{-1}$ pc$^{-2}$) | log $F$ (ergs s$^{-1}$ cm$^{-2}$) | log $L$ (ergs s$^{-1}$) |
|---|---|---|---|---|---|---|---|
| 86 ..... | 230.0 | 11.4 | 36.2 | 24.4 | 34.32 | −13.58 | 37.89 |
| 89 ..... | 211.4 | 14.8 | 56.3 | 32.8 | 34.55 | −13.10 | 38.37 |
| 108 ..... | 225.6 | 14.9 | 63.0 | 32.0 | 34.82 | −12.84 | 38.63 |
| 114 ..... | 233.4 | 13.4 | 68.0 | 37.0 | 34.66 | −12.88 | 38.59 |
| 119 ..... | 217.9 | 12.1 | 67.2 | 35.5 | 34.71 | −12.87 | 38.61 |
| 128–129..... | 223.5 | 24.3 | 50.5 | 37.9 | 34.18 | −13.34 | 38.13 |
| 132 ..... | 225.6 | 13.7 | 84.6 | 39.1 | 35.04 | −12.46 | 39.02 |
| 133 ..... | 207.2 | 15.8 | 74.4 | 35.9 | 34.95 | −12.62 | 38.86 |
| 146 ..... | 215.7 | 21.6 | 94.4 | 65.4 | 34.28 | −12.76 | 38.71 |
| 149 ..... | 208.6 | 37.9 | 63.8 | 40.5 | 34.40 | −13.06 | 38.41 |
| 151 ..... | 222.9 | 28.1 | 76.8 | 48.3 | 34.41 | −12.89 | 38.58 |
| 153–159..... | 215.3 | 27.4 | 74.3 | 50.0 | 34.32 | −12.96 | 38.52 |
| 178–190..... | 223.6 | 31.1 | 75.8 | 64.4 | 34.04 | −13.01 | 38.46 |
| 191 ..... | 203.8 | 17.8 | 51.5 | 36.4 | 34.23 | −13.32 | 38.15 |
| 203 ..... | 192.3 | 21.7 | 86.1 | 54.2 | 34.39 | −12.82 | 38.65 |
| 208 ..... | 196.8 | 21.9 | 60.5 | 33.3 | 34.64 | −13.00 | 38.48 |
| 210 ..... | 225.3 | 40.4 | 30.5 | 24.1 | 34.11 | −13.80 | 37.67 |
| 212 ..... | 214.2 | 20.5 | 72.7 | 42.7 | 34.50 | −12.92 | 38.56 |
| 220 ..... | 188.4 | 17.7 | 94.7 | 43.0 | 35.09 | −12.32 | 39.15 |
| 222 ..... | 210.9 | 23.0 | 127.2 | 62.2 | 34.89 | −12.20 | 39.27 |
| 223 ..... | 194.3 | 29.5 | 37.8 | 27.5 | 34.20 | −13.60 | 37.88 |
| 226 ..... | 207.2 | 21.1 | 125.4 | 63.1 | 34.82 | −12.26 | 39.22 |
| h 66 ..... | 200.6 | 23.1 | 120.9 | 58.1 | 34.93 | −12.22 | 39.26 |
| Nucleus..... | 230.9 | 27.9 | 155.2 | 69.3 | 35.15 | −11.84 | 39.63 |

NOTE.—Columns are same as in Table 4.

culated for both emission lines using the $R$ radius. This is the radius that would be observed if the luminosity profiles did not overlap and if the diffuse luminosity of NGC 4449 did not exist, and so it is more convenient to compare our results with those published in the literature. The distribution functions for Hα and [O III] are shown in Figure 9.

In both plots, the exponential $N = N_0 e^{-D/D_0}$ fit proposed by van den Bergh (1981) is satisfactory, giving confidence about the method used to determine the integrated H II region parameters. The fit was made by discarding the points corresponding to diameters smaller than 4″ because of the observed deficit of nebulae below this value, due basically to the intense diffuse emission of this galaxy (which prevents the detection of the smallest regions) and to the relatively low sensitivity of the detector used. The fitting parameters are $N_0 = 328$ and $D_0 = 1\farcs6$ for the Hα data and $N_0 = 141$ and $D_0 = 2\farcs4$ for [O III].

In the galaxy sample studied by Hodge (1983), NGC 4449 is one of the galaxies that presents a poorer fit to the van den Bergh law (see his Fig. 1). In our plot, the fit is considerably more satisfactory than in Hodge's work or in that published by Sabbandin & Bianchini (1979)—also shown in Figure 1 in Hodge's article. Both studies show an important relative excess of small H II regions, presumably due to their visual size determination.

Given that our observations cover just the central portion of this galaxy, care must be taken when comparing our results with Hodge's (1983) and Sabbandin & Bianchini's (1979), since their observations cover the whole galaxy. If, in the diameter distribution function by Sabban-

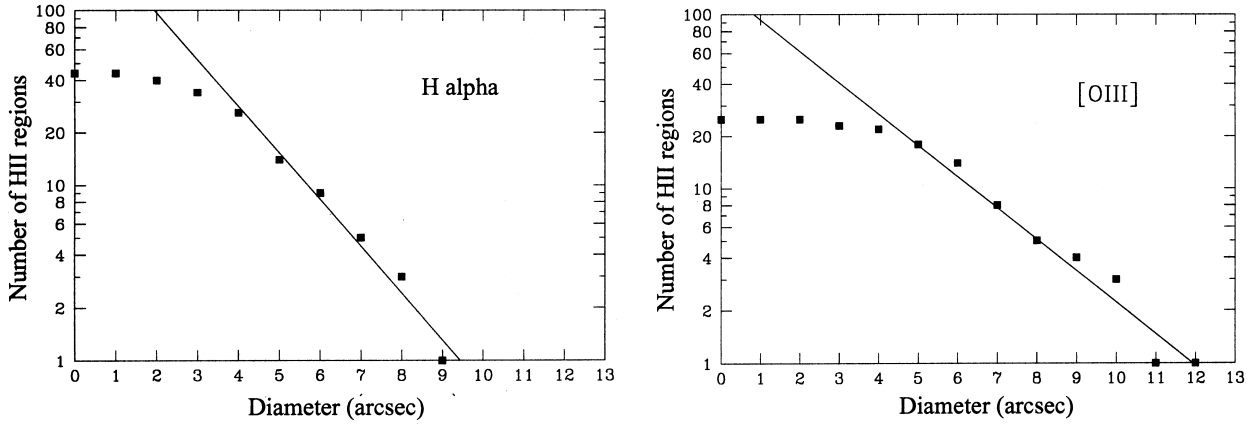


FIG. 9.—Accumulated diameter distribution functions for the H II regions in the central 80″ × 80″ of NGC 4449. The diameters were determined by extrapolating the visible part of the nebular luminosity profiles.

din & Bianchini, the smaller H II regions ($D < 4$ pc) are discarded, the values obtained are $N_0 = 30$ and $D_0 = 6''.2$. But if we use only those nebulae with diameters between 3″ and 9″ (the part of their data that better fits a van den Bergh law), we find $N_0 = 106$ and $D_0 = 2''.8$, which is compatible with our [O III] results. Hodge's values are $N_0 = 115$ and $D_0 = 5''.5$.

We also calculated the H II region luminosity function for the two observed emission lines (see Fig. 10). Luminosity functions can be adjusted by an $N(L) = AL^a dL$ law (Kennicutt et al. 1989), where $N(L)$ is the number of nebulae with a luminosity between $L$ and $L + dL$. In our case, only the brightest nebulae follow this law, surely because of the difficulty in detecting the faintest H II regions. It must also be taken into account that our data cover only a part of the galaxy and that this part is especially rich in giant H II regions. The fitted regression lines, using only the most luminous H II regions (where the plots display a negative slope) lead to the exponent $a = -1.9$ for Hα, while for the [O III] data $a = -1.6$. In both cases, and especially for the [O III] data, the fit is just marginally reliable because of the relatively low number of nebulae in our sample.

Kennicutt et al. (1989), using Hα images that cover the whole area of NGC 4449, found $a = -1.48$ (see their Fig. 17). The mean value they publish for galaxies with the same morphological type as NGC 4449 is $a \sim (-1.7)$. This small discrepancy suggests an excess of luminous H II regions for NGC 4449 relative to other galaxies of similar type, which can be related to the abnormally high proportion of nebulae displaying a supersonic velocity width in this galaxy.

The differences between Kennicutt's luminosity function and ours are due to several causes. Apart from the lower sensitivity of our detector and the fact that our observations cover only the central portion of this galaxy, the most important factor is the lower spatial resolution in the data of Kennicutt et al. (1989). Their images possess a nominal angular resolution of 2″, which was further degraded to have the same resolution in all the galaxies of their sample. As these authors show, a low resolution, combined with the high surface density of H II regions in NGC 4449, gives rise to a luminosity function that is flatter than the real one. In fact, according to Kennicutt and collaborators the average diameter for the three larger H II regions in this galaxy is 400 pc, while in our case it is only about 200 pc.

## 6. SUMMARY AND CONCLUSIONS

Using two-dimensional Fabry-Perot spectroscopy taken in the emission lines of Hα and [O III] λ5006.8 Å, we have produced continuum-free emission, radial velocity, and velocity dispersion maps for the central portion of the irregular galaxy NGC 4449. Both emission lines show basically the same structures. To build these maps, we have defined useful new criteria that can be applied to any Fabry-Perot data cube, allowing the global S/N to be increased and areas with low, unreliable signals to be eliminated.

The radial velocity maps display a nonsystematic structure, with no suggestion of rotation and with differences up to 50 km s$^{-1}$ between areas separated by some 200 pc. The total range of observed radial velocities is some 60 km s$^{-1}$. The turbulent velocity dispersion maps show that H II regions possess velocity widths between 10 and 20 km s$^{-1}$, significantly lower than the intercloud medium, with corresponding values between 20 and 50 km s$^{-1}$.

The presence of an intense, morphologically diffuse luminosity in this galaxy, as well as its high nebular surface density, prevents the use of usual methods to detect and measure H II regions. Because of this, a new method has been developed to find nebulae in bright, nonhomogeneous backgrounds and to obtain objective and precise estimates of their sizes. This method will be useful for studying H II region populations in other irregular galaxies or in especially crowded areas in spiral arms.

The accumulated diameter distribution function obtained with the new size definition follows a van den Bergh law more closely than those published to date for NGC 4449, confirming the usefulness and precision of the adopted procedure. The average diameters of the largest regions are about 200 pc, smaller than previously reported. This size is probably related to the disc thickness of the galaxy. Similar values have been deduced by means of a completely different argument, for example in the Magellanic irregular NGC 4214 (see Muñoz-Tuñón et al. 1998; Maiz-Apellaniz et al. 1999).

Forty-four H II regions in Hα and 24 in [O III] have been cataloged. The difference is due to the slightly different areas covered by the observations in each emission line and to the fact that some nebulae do not show measurable emission in [O III] above the diffuse luminosity of this galaxy.

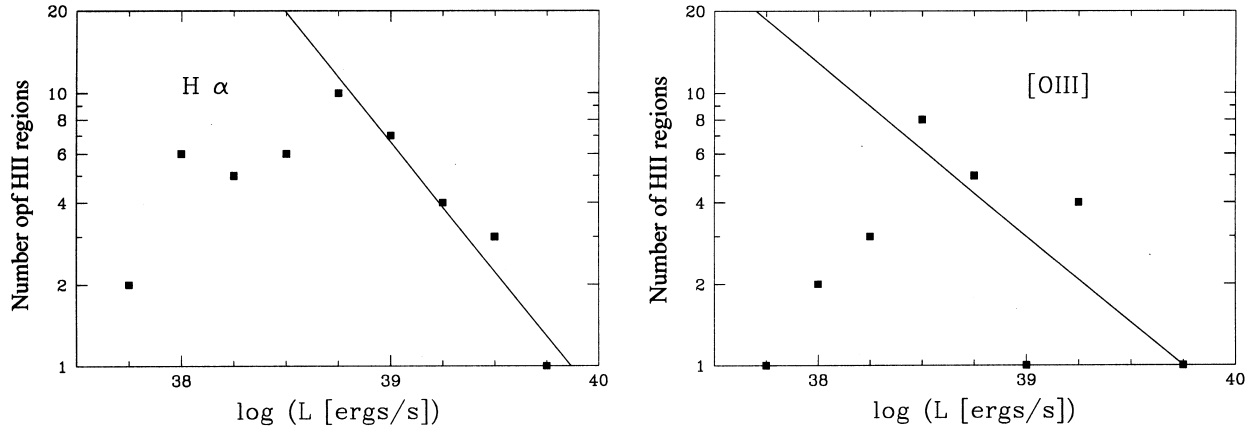


FIG. 10.—H II region luminosity function in Hα and [O III] for the nebulae detected in NGC 4449

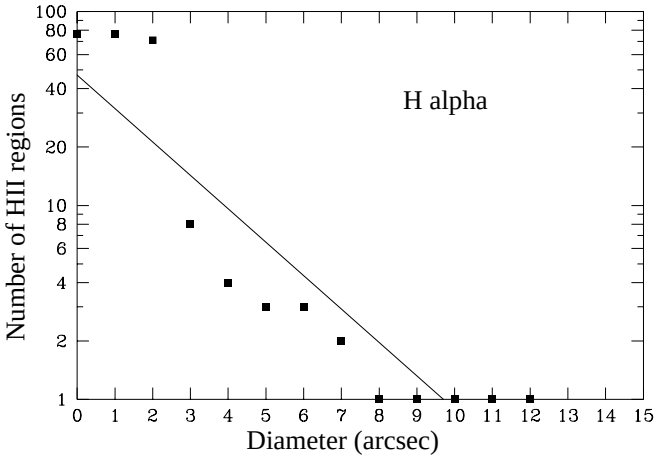


FIG. 11.—H II region diameter distribution function (visually determined) for the Hα data. The straight line is the fit to the data.

We have obtained linear diameters, luminosities, surface brightnesses, radial velocities, and velocity dispersions for all these nebulae. The relationships among these parameters will be the subject of a forthcoming paper.

This study was partly financed by the Spanish DGES (grant PB97-0158). We express our thanks to Guillermo Tenorio-Tagle for his comments and fruitful discussions. The William Hershel Telescope and Jacobus Kapteyn Telescope are operated on the island of La Palma by the Isaac Newton Group at the Observatorio del Roque de los Muchachos of the IAC. Thanks are due to the IAC's scientific editorial service for linguistic and stylistic corrections to the text. Many thanks are also given to our anonymous referee for his or her help and constructive comments.

## APPENDIX

## METHODS FOR OBTAINING INTEGRATED H II REGION PARAMETERS APPLIED TO NGC 4449

In this appendix, the different methods described in § 1 to obtain the integrated H II region parameters will be checked when applied to NGC 4449. The most basic parameter is size, since it determines the area on the images where the luminosity is measured and where the spectra are averaged to get the integrated velocity dispersion and radial velocity. We will not show the results of the isophotal method proposed by Kennicutt (1979), because when applied to the Hα continuum-free flux image (Fig. 1, *left*; Fig. 2, *left*), the isophotal value corresponding to H II region halos encloses the main body of the galaxy, thereby preventing the use of this method in assigning sizes to nebulae.

### A1. VISUAL DIAMETER DETERMINATION

Using this method, the size of each H II region detected in the continuum-free flux images (Figs. 1 and 2) was obtained. Each nebula was assigned the diameter corresponding to a circular area with the same surface as the extension (visually determined) covered by the emission in our images. When an H II region was located in the data cube overlapping area, the two respective sizes were determined and averaged.

By means of this procedure, 77 H II regions were measured in the Hα and 79 in the [O III] data cubes. The difference is due to the fact that the field covered by the observations in each emission line was not exactly the same and to the undetectability in some of the wavelengths in some of the faintest or smallest H II regions where the diffuse emission was most intense or where the surface density of nebulae was highest. Some of the lowest surface brightness H II regions found by Sabbandin & Bianchini (1979) or Hodge (1969) were not detected in our data because of the relatively lower sensitivity of our detector.

It must be pointed out that this method presents important problems when applied to a galaxy like NGC 4449, which became evident during the process of measuring diameters. Faint or irregularly shaped H II regions are subjectively detected and/or measured with difficulty in this way, especially when they are located in areas of intense diffuse emission or where the surface density of nebulae is high.

The resultant diameter distribution function (shown in Fig. 11) strongly suggests that this method is not reliable when applied to galaxies with the characteristics of NGC 4449. This function should follow an approximately exponential law of the form $N = N_0 e^{-D/D_0}$, as proposed by van den Bergh (1981). However, our data show an important deviation, with a considerable relative excess of small (diameters less than 3″) H II regions, most probably because the diffuse emission and the overlapping of luminosity profiles for neighboring H II regions do not allow detection of the dim outskirts of many nebulae in our sample. This result is similar to that published by Sabbandin & Bianchini (1979) and Hodge (1983) following the same method for this galaxy.

### A2. SIZE DETERMINATION BASED ON RADIAL VELOCITY AND VELOCITY DISPERSION GRADIENTS

This method is based on the separation of adjacent H II regions following their kinematic characteristics. In this way, if they present clearly different radial velocities or velocity dispersions, this will strongly suggest that we are dealing with physically independent nebulae. This method could in principle allow H II region size determination as the extension of more or less constant radial velocities and velocity dispersions in the maps.

The best way to visualize and quantify radial velocity and velocity dispersion spatial variations is by means of maps displaying the gradients of these two parameters. With this aim, we used the routine IDIFF in the FIGARO package, which substitutes the value $f(x, y)$ of each pixel in a two-dimensional image for

$$\frac{|f(x, y) - f(x-1, y)|}{4} + \frac{|f(x, y) - f(x, y-1)|}{4} + \frac{|f(x, y) - f(x+1, y)|}{4} + \frac{|f(x, y) - f(x, y+1)|}{4}.$$

The resulting maps, both in Hα and in [O III], and both the radial velocity and velocity dispersion ones, have a very similar appearance. Comparing them with the continuum-free emission maps, we determined that actual H II regions correspond to areas in the gradient maps with values of

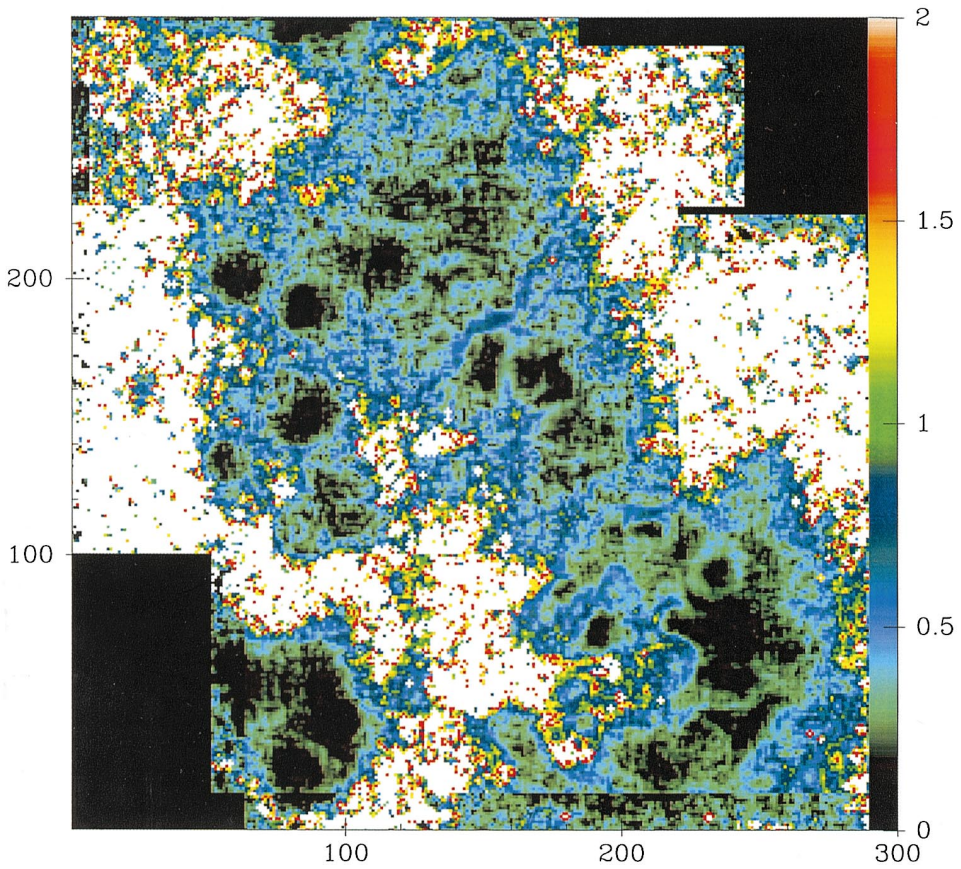


FIG. 12.—Composite map made with the velocity dispersion and radial velocity gradient maps for the two observed emission lines. Color code units are km $s^{-1}$ $pixel^{-1}$. Each pixel corresponds to some 6 pc.

$\sim$0.1 km $s^{-1}$ $pixel^{-1}$. Adjacent nebulae are usually separated by gradients in both magnitudes of the order of 0.5 km $s^{-1}$ $pixel^{-1}$. The separation between H II regions and the intercloud medium is given by high values ($>1$ km $s^{-1}$ $pixel^{-1}$) of radial velocity and velocity dispersion gradients because of the low S/N in the intercloud medium, which gives rise to randomly changing kinematic values. In Figure 12, we show a mosaic made with the velocity dispersion and radial velocity gradient maps for the four data cubes, built like this to capture the clearest parts of each map.

Each nebula was assigned the diameter corresponding to a circular area with the same surface as the extension covered by gradient values lower than 0.1 km $s^{-1}$ $pixel^{-1}$ in the images that displayed the average of the radial velocity and velocity dispersion gradient for each emission line. The limits selected for each H II region were those for which the gradient value was $\gtrsim$0.5 km $s^{-1}$ $pixel^{-1}$. When an H II region was located in the data cube overlapping area, the two respective sizes were determined and averaged. Using this method, 33 nebulae in each emission line were detected.

This method allows the objective separation of some of the adjacent H II regions, but no precise size determination is obtained. It must be borne in mind that if the integration time had been longer, the S/N in the areas that present high gradients would have improved (especially in the frontiers between H II regions and the intercloud medium), so the spatial variations of the kinematic parameters would have been lower, and consequently the H II region limits would have been different. Besides, as can be seen in Figure 12, only a few nebulae present well-defined limits, while for the rest size determination is as subjective a task as when it was done visually on the continuum-free emission maps.

Again, a clear indication of the unsuitability of this method for a galaxy like NGC 4449 was given by the diameter distribution function, shown in Figure 13. The fit to a van den Bergh law (shown in the figure) is also quite poor. In this case, the most significant discrepancies are found for intermediate-diameter values (between $\sim$5″ and $\sim$15″), for which it is not possible to fit a single regression line. If the fit

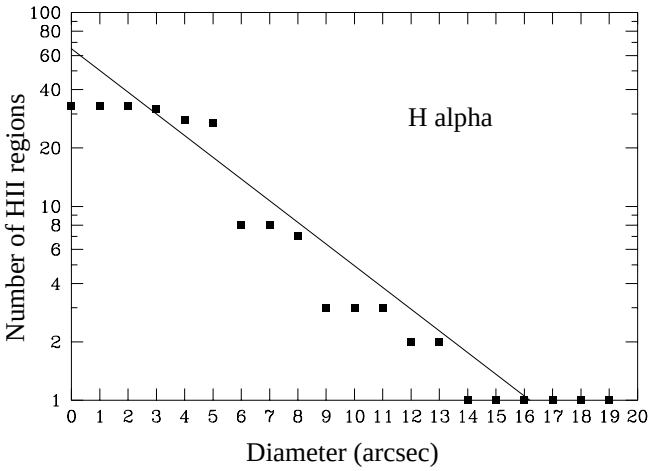


FIG. 13.—Diameter distribution function for the H II regions detected in H$\alpha$. Diameters were determined by means of the radial velocity and velocity dispersion gradients.

is made using the larger diameter values (between 9″ and 19″), we find a relative excess of small nebulae (diameter $<9''$), probably because the diffuse gas, which possesses kinematic parameters different from those in H II regions, dominates the emission in the faint outskirts of nebulae. If, alternatively, the fit is made using the smaller H II regions, (between $\sim 4''$ and $\sim 10''$), a relative excess of large ($>10''$) nebulae is found because of the small differences in the kinematic parameters of some adjacent nebulae that appear as a single H II region in the gradient maps.

### A3. SIZE DETERMINATION BY MEANS OF THE FOCAS PACKAGE

One of the most important problems in the previous methods is the subjectivity in size determination. To get rid of this effect, we used the FOCAS package developed within the IRAF package by F. Valdez at Kitt Peak National Observatory. FOCAS analyzes images (in our case, the continuum-free flux maps) by finding the relative maxima of emission, but only if their emission is higher than the local background plus a certain number of times its standard deviation and only if the detected area has a certain minimum number of pixels. In our case, the optimum parameters were a threshold of 3 times the local background standard deviation and a minimum area of 7 pixels (comparable to the seeing disk). This procedure is somewhat similar to the isophotal diameters by Kennicutt (1979), with the advantage of using a different isophotal level for each nebula, slightly higher than the diffuse luminosity, since the luminosity profile of this emission is much smoother than those of the H II regions, and so FOCAS identifies it as local background.

Once the relative maxima are detected, FOCAS provides their position, average level of the corresponding lower (limiting) isophote, and the area and flux enclosed. The resulting catalog was compared with those by Sabbandin & Bianchini (1979) and Hodge (1969) to identify the detected H II regions. This comparison revealed that some of the faintest FOCAS detections were spurious, corresponding to the brightest parts in the diffuse luminosity. To discard them, the relative maxima with a flux of less than 16 counts in Hα or 30 in [O III] were removed from the list, as well as the detections corresponding to the ghost reflections. Finally, 48 nebulae were positively identified in Hα and 39 in [O III], and their diameters were determined from the area assigned by FOCAS to each of them.

This method avoids the subjectivity in the detection and measurement of nebulae and reduces the problem of the diffuse luminosity in NGC 4449. However, the size determination in the zones of high surface density of nebulae is still wrong, since when the luminosity profiles overlap, FOCAS logically detects their brightest, nonoverlapped parts, although the faint wings of these luminosity profiles would enclose larger areas.

The diameter distribution function (shown in Fig. 14) gives a better global fit to the van den Bergh law than the previous cases. Discrepancies are still present (although they are less systematic), especially in the range of diameters between 3″ and 5″. The fact that FOCAS underestimates the H II region sizes when their luminosity profiles overlap is reflected in the diameter values, globally smaller than those found with previous methods.

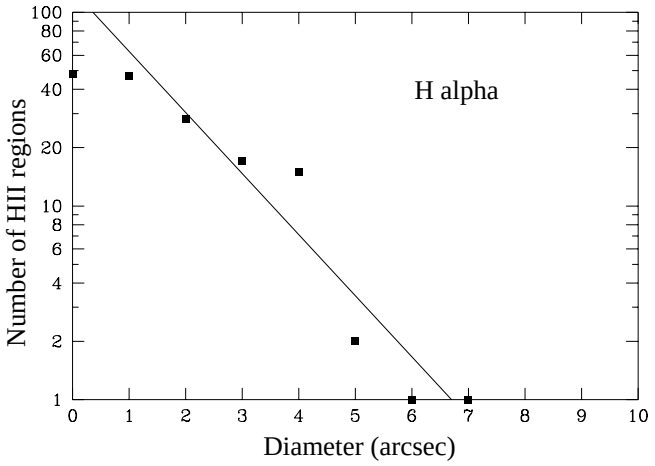


FIG. 14.—Diameter distribution function for the H II regions detected by FOCAS in the continuum-free Hα images.

## REFERENCES


Aaronson, M., & Mould, J. 1983, ApJ, 265, 1
Bland, J., Taylor, K., & Atherton, P. D. 1987, MNRAS, 228, 595
Bothun, G. D. 1986, AJ, 91, 507
Burstein, D., & Heiles, C. 1978, ApJ, 225, 40
Gallagher, J. S., & Hunter, D. A. 1983, ApJ, 274, 141
Gallagher, J. S., Hunter, D. A., & Tutukov, A. V. 1984, ApJ, 284, 544
Gavryusev, V., & Muñoz-Tuñón, C. 1996, in ASP Conf. Ser. 101, Astronomical Data Analysis Software and Systems V, ed. G. H. Jacoby & J. Barnes (San Francisco: ASP), 76
Hartmann, L. W., Geller, M. J., & Huchra, J. P. 1986, AJ, 92, 1278
Hill, R. S., Home, A. T., Smith, A. M., Bruhweiler, F. C., Cheng, K. P., Hintzen, P. M. N., & Oliversen, R. J. 1994, ApJ, 430, 568
Hippelein, H. 1986, A&A, 160, 374
Hodge, P. W. 1969, ApJS, 18, 73
———. 1976a, ApJ, 205, 728
———. 1976b, R. Obs. Bull., 182, 169
———. 1983, AJ, 88, 1323
Hunter, D. A. 1982, ApJ, 260, 81
———. 1984, ApJ, 276, L35
Hunter, D. A., & Gallagher, J. S. 1986, PASP, 98, 5
———. 1997, ApJ, 475, 65
Kennicutt, R. C. 1979, ApJ, 228, 394
———. 1984, ApJ, 287, 116
———. 1988, ApJ, 334, 144
———. 1992, ApJ, 388, 310
Kennicutt, R. C., Edgar, B. K., & Hodge, P. W. 1989, ApJ, 337, 761
Knapen, J. H., Arnth-Jensen, N., Cepa, J., & Beckman, J. E. 1993, AJ, 106, 56
Lewis, J., & Unger, S. 1991, William Hershel Telescope: Taurus Data and How to Reduce It (La Palma: Obs. Roque de los Muchachos)
Maiz-Apellaniz, J., Muñoz-Tuñón, C., Tenorio-Tagle, G., & Mas-Hesse, M. 1999, A&A, 343, 64
Malumuth, E. M., Williams, T. B., & Schommer, R. A. 1986, AJ, 91, 1295
Melnick, J. 1977, ApJ, 213, 15
———. 1979, ApJ, 228, 112
Muñoz-Tuñón, C. 1994, in Violent Star Formation: From 30 Doradus to QSOs, ed. G. Tenorio-Tagle (Cambridge: Cambridge Univ. Press), 25
Muñoz-Tuñón, C., Fuentes-Masip, O., & Castañeda, H. O. 1998, Publ. Astron. Soc. Australia, 15, 103
Muñoz-Tuñón, C., Tenorio-Tagle, G., Castañeda, H. O., & Terlevich, R. 1996, AJ, 112, 1636
Sabalisck, N. S. P., Tenorio-Tagle, G., Castañeda, H. O., & Muñoz-Tuñón, C. 1995, ApJ, 444, 200
Sabbandin, F., & Bianchini, A. 1979, PASP, 91, 280
Sabbandin, F., Ortolani, S., & Bianchini, A. 1984, A&A, 131, 1
Sandage, A. 1961, The Hubble Atlas of Galaxies (Washington: Carnegie Inst. Washington)
Sandage, A., & Tammann, G. A. 1974, ApJ, 190, 525
———. 1975, ApJ, 196, 313
———. 1981, A Revised Shapley-Ames Catalog of Bright Galaxies (Washington: Carnegie Inst. Washington)
Sasaki, M., Ohta, K., & Saito, M. 1990, PASJ, 42, 361

Scowen, P. A. 1992, Ph.D. thesis, Rice Univ.
Smith, M. G. 1977, in IAU Colloq. 37, Décalage vers le rouge et expansion de l'univers, ed. C. Balkowski & B. E. Westerlund (Paris: Editions du CNRS), 75
Smith, M. G., & Weedman, D. W. 1970, ApJ, 161, 33
———. 1971, ApJ, 169, 271
Taylor, K., & Atherton, P. D. 1980, MNRAS, 191, 675
Thronson, H. A., Jr., Hunter, D. A., Telesco, C. M., Decher, R., & Harper, D. A. 1987, AJ, 317, 180
van den Bergh, S. 1981, AJ, 86, 1464
Yoshida, M., Shimizu, Y., Koyano, H., Kosugi, G., Aoki, K., Ohtani, H., Sasaki, T., & Sasaki, M. 1995, in ASP Conf. Ser. 71, Tridimenional Optical Spectroscopic Methods in Astrophysics, ed. G. Comte & M. Marcelin (San Francisco: ASP), 207